Chapter 6

Palladium In A Pure Oxygen Gas Phase

6.1 Oxidation Stages Of Pd(100)

The structure and composition of a surface can be altered significantly depending on the surrounding gas phase conditions. In the particular case of a metal surface in contact with a pure oxygen gas phase it is usually expected, that with increasing oxygen content in the gas phase the surface will eventually be oxidized, which can be preceded by several stages of oxygen adlayers or so-called surface oxides. In this context the term *surface oxide* is mostly used for structures, that are more complex than a simple, ordered, on-surface adlayer, but still only represent a sub-nanometer thin film of an oxide-like structure on the metal surface.

The oxidation of the Pd(100) surface is a complex process, passing through several stages. Experimentally, four different phases have been observed, when exposing the Pd(100) surface to oxygen [109–113]. These include a $p(2 \times 2)$, a $c(2 \times 2)$, a (5×5) and a $(\sqrt{5} \times \sqrt{5})R27°$ structure. In a last stage the surface roughens and bulk palladium oxide (PdO) is formed. In this Section the geometric structures of the different phases are briefly discussed. Here, the (5×5) phase has not been considered, since the structure and state of the oxygen atoms has not been well established so far, i.e. there exists no well defined structural model. In addition, the (5×5) phase appears to be only of metastable character. The formation of a (5×5) structure is very sensitive to the surface preparation and oxygen exposure range, so that in the oxidation as well as in the reduction process the (5×5) structure can be bypassed going directly from a (2×2) to a $(\sqrt{5} \times \sqrt{5})R27°$ structure and vice versa [113].

Clean Metal Surface

Palladium is a late $4d$ transition metal, that crystallizes in the face-centered cubic (fcc) structure. The experimentally determined lattice constant at $T = 298\,\mathrm{K}$ is $a_0 = 3.880\,\mathrm{Å}$ [11]. For the setup of the different Pd(100) surface structures, though, the
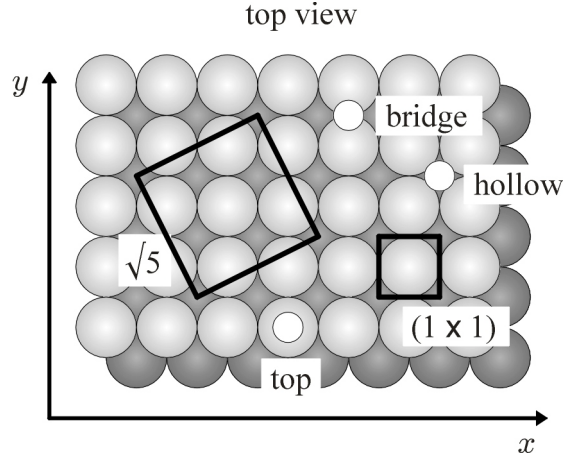
top view

Figure 6.1: Schematic illustration of the Pd(100) surface. In addition to the different adsorption sites (white circles) the $(\sqrt{5} \times \sqrt{5})R27°$ and (1×1) surface unit cells are indicated.

	PBE	RPBE	LDA	Exp. [11]
Pd-fcc, bulk, a_0	3.95	3.99	3.84	3.880
(1×1)-Pd(100), $a_0/\sqrt{2}$	2.79	2.82	2.71	2.744
$(\sqrt{5} \times \sqrt{5})R27°$-Pd(100), $a_0\sqrt{5}/\sqrt{2}$	6.24	6.31	6.07	6.135

Table 6.1: Optimized cubic lattice constant of Pd obtained within the PBE, RPBE and LDA approximation for the exchange-correlation functional. For comparison also the experimental value is given. The experimental value is measured at $T = 298\,\mathrm{K}$, whereas the theoretical results are given at $T = 0\,\mathrm{K}$ without ZPV. In addition the resulting surface unit cell length of of the (1×1) and $(\sqrt{5} \times \sqrt{5})R27°$ structures are shown. All values are in Å.

theoretically optimized lattice constants are used. Since the theoretically determined lattice constant usually deviates slightly from the experimental one, the use of the experimental lattice constant could induce lateral strain effects. The results for the equilibrium lattice constant are listed in Tab. 6.1 for the PBE, the RPBE and the LDA as approximation to the exchange-correlation functional (cf. Section 2.5). The values have been obtained within the FP-(L)APW+lo approach (cf. Chapter 3) using the WIEN2k-code [67]. The muffin-tin radius for palladium is set to $R_{\mathrm{MT}}^{\mathrm{Pd}} = 2.0\,\mathrm{bohr}$, the wave function expansion inside the muffin-tins is considered up to $l_{\max}^{\mathrm{wf}} = 12$, and the potential expansion up to $l_{\max}^{\mathrm{pot}} = 6$. The Brillouin zone (BZ) integration is performed using a $[10 \times 10 \times 10]$ Monkhorst-Pack (MP) grid [61]. The energy cutoff for the plane wave representation in the interstitial region is $E_{\max}^{\mathrm{wf}} = 20\,\mathrm{Ry}$ for the wave function and $E_{\max}^{\mathrm{pot}} = 196\,\mathrm{Ry}$ for the potential (a detailed discussion of the convergence with respect to the chosen parameters in given in Appendix A).

In addition to the optimized bulk lattice constant the length of the resulting surface unit cell vectors of a simple (1×1) and the $(\sqrt{5} \times \sqrt{5})R27°$ structure are shown. As
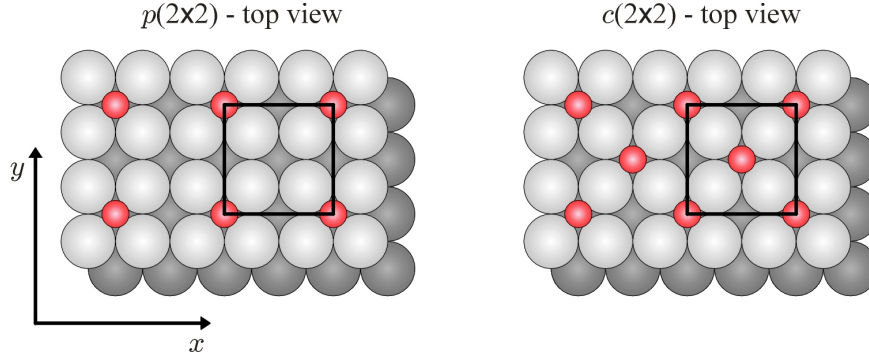
Figure 6.2: Schematic illustration of the $p(2 \times 2)$ (left) and $c(2 \times 2)$ (right) adlayer structures on Pd(100). The small, red spheres indicate oxygen atoms, large, light-grey ones are Pd atoms, and Pd atoms in the second layer are darkened.

expected, the LDA values reflect an overbinding tendency resulting in a $\sim 1\%$ smaller lattice constant compared to the experimental value, whereas the gradient corrected functionals overcorrect the LDA leading to ~ 2–3% too large lattice constants. For the results presented in this work the surface unit cells are constructed using the respective optimized lattice constant for each functional.

In Fig. 6.1 a schematic representation of the Pd(100) surface is shown. The surface exhibits three different, high-symmetry adsorption sites, a bridge, a top and a hollow site. Also the surface unit cells of the (1×1) and the $(\sqrt{5} \times \sqrt{5})R27°$ structure are indicated.

Adlayers

Exposing the Pd(100) surface to an oxygen gas phase leads in the first stage to the formation of adlayer structures. Depending on the temperature and pressure conditions of the oxygen gas phase a variety of ordered and disordered structures might occur. This study, however, will focus in a first approach only on the two experimentally characterized ordered adlayers, the $p(2 \times 2)$ and the $c(2 \times 2)$. In both structures the oxygen atoms are adsorbed in the fourfold hollow site with a coverage of 0.25 monolayers (ML) and 0.5 ML, respectively. A top view of the two structures is shown in Fig. 6.2. The $c(2 \times 2)$ structure is also referred to as checkerboard pattern.

Surface Oxide

A further oxidation of the Pd(100) surface results in the formation of a $(\sqrt{5} \times \sqrt{5})R27°$ structure accompanied by a reconstruction of the topmost palladium layer. A detailed experimental and theoretical investigation by Todorova *et al.* [18] revealed, that the structure of the $(\sqrt{5} \times \sqrt{5})R27°$ surface oxide can essentially be described by a PdO(101) overlayer on Pd(100). The surface unit cell contains four palladium and four oxygen atoms on-top of five Pd(100) substrate atoms, cf. Fig 6.3. The four
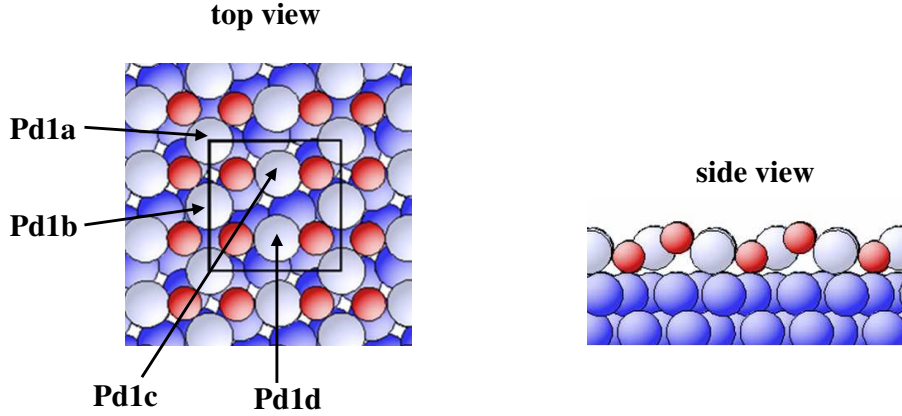
top view

side view

Figure 6.3: Schematic illustration of the $(\sqrt{5} \times \sqrt{5})R27°$ surface oxide structure on Pd(100). The small, red circles indicate oxygen atoms, the large, light-blue ones Pd atoms in the reconstructed oxide layer and the dark blue ones Pd atoms of the Pd(100) substrate.

palladium atoms can be divided into two groups, two of them are fourfold (Pd1a and Pd1b) and two are twofold (Pd1c and Pd1d) coordinated by oxygen atoms. Also the four oxygen atoms split into two groups, two of them sit at the interface between the surface oxide layer and the substrate and two on-top of the topmost palladium layer. Because of this oxide-like trilayer structure the $(\sqrt{5} \times \sqrt{5})R27°$ is considered as a surface oxide rather than a simple adlayer.

Bulk Oxide

Exposing the Pd(100) surface to an even higher oxygen pressure it has been observed experimentally, that in a last stage of the oxidation process the surface will finally be fully oxidized and bulk-like PdO forms on the surface. The oxide formation induces a substantial restructuring of the surface, which is indicated by an increasing roughness during the oxidation process [23, 113].

Palladium oxide crystallizes in the tetragonal PtS-structure with space group D_{4h}^9 [114]. Each Pd atom is planar coordinated by four oxygen atoms and each O atom is tetrahedrally surrounded by four Pd atoms. The tetragonal unit cell contains two PdO units with Pd atoms at all corners and in the center, and oxygen atoms at (0, 1/2, 1/4), (0, 1/2, 3/4) resp. (1, 1/2, 1/4), (1, 1/2, 3/4), cf. Fig. 6.4. Also for the palladium oxide the lattice constants are optimized individually for every exchange-correlation functional. The experimental lattice constants at room temperature are $a_0 = 3.043\,\text{Å}$ and $c_0 = 5.336\,\text{Å}\,(c/a = 1.753)$ [114]. The calculated values are compiled in Tab. 6.2. Again, the LDA overestimates the binding energy giving slightly too small lattice constants (~ 0.8–$1.7\,\%$), whereas the gradient corrected functionals yield slightly too large lattice constants (~ 0.3–$3.5\,\%$).

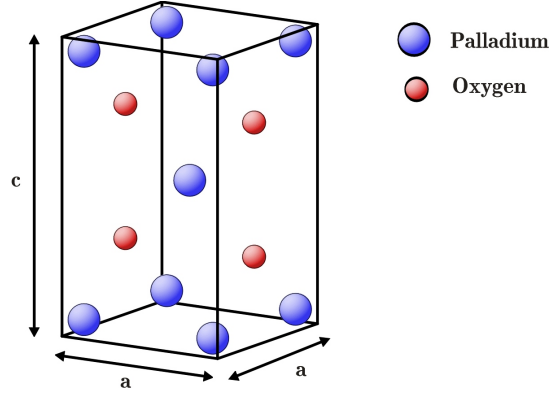The values have been obtained using the following parameters: muffin-tin radii for

Figure 6.4: Tetragonal unit cell of PdO.

	PBE	RPBE	LDA	Exp. [114]
PdO a_0 (Å)	3.05	3.09	2.99	3.043
PdO c_0 (Å)	5.50	5.53	5.29	5.336
PdO c/a	1.80	1.79	1.77	1.753

Table 6.2: Optimized lattice constants for the tetragonal unit cell of PdO obtained within the PBE, RPBE and LDA approximation for the exchange-correlation functional. For comparison also the experimental values are given. The experimental values are measured at room temperature, whereas the theoretical results are are given $T = 0\,\mathrm{K}$ without ZPV.

palladium $R_{\mathrm{MT}}^{\mathrm{Pd}} = 1.8\,\mathrm{bohr}$ and oxygen $R_{\mathrm{MT}}^{\mathrm{O}} = 1.3\,\mathrm{bohr}$, wave function expansion inside the muffin tins up to $l_{\max}^{\mathrm{wf}} = 12$ and potential expansion up to $l_{\max}^{\mathrm{pot}} = 6$. A $[12 \times 12 \times 7]$ MP-grid is used for the BZ integration and the energy cutoff for the planewave representation in the interstitial is $E_{\max}^{\mathrm{wf}} = 20\,\mathrm{Ry}$ for the wave function and $E_{\max}^{\mathrm{pot}} = 196\,\mathrm{Ry}$ for the potential (a detailed discussion of the convergence with respect to the chosen parameters in given in Ref. [115]).

6.2 Atomistic Thermodynamics - Stability In Thermodynamic Equilibrium With An O$_2$ Gas Phase

In the previous Section the geometric structures of the different oxidation stages of the Pd(100), that will be considered in this work, have been introduced shortly. In this Section the atomistic thermodynamics approach (cf. Chapter 4) is applied to evaluate the stability of these different phases in thermodynamic equilibrium with an oxygen gas phase. The atomistic thermodynamics approach appears to be most suitable at this point, since this Section only focuses on the comparison of the stability of already

known structures. Also, kinetic effects in the oxidation process are not considered here, but only the final, thermodynamic stable phases are investigated.

As a quantity to compare the stability of the different phases the Gibbs free energy of adsorption ΔG^{ads} is used as defined in Eq. (4.29). In a first approach the Gibbs free energies of the different subsystems are approximated by the total energies, which are the leading terms and directly accessible by DFT calculations. The contributions of the remaining terms to the Gibbs free energy will be discussed below. Using only the total energies, the Gibbs free energy of adsorption for the different oxidation stages of the Pd(100) surface is then determined by

$$\Delta G^{\mathrm{ads}}(\Delta\mu_{\mathrm{O}}) = -\frac{1}{A}\left(E^{\mathrm{tot}}_{\mathrm{O@Pd(100)}} - E^{\mathrm{tot}}_{\mathrm{Pd(100)}} - \Delta N_{\mathrm{Pd}}E^{\mathrm{tot}}_{\mathrm{Pd,bulk}} - N_{\mathrm{O}}(1/2 E^{\mathrm{tot}}_{\mathrm{O}_2} + \Delta\mu_{\mathrm{O}})\right)$$

$$= -\frac{N_{\mathrm{O}}}{A}\widetilde{E}^{\mathrm{bind}}_{\mathrm{O@Pd(100)}} + \frac{N_{\mathrm{O}}}{A}\Delta\mu_{\mathrm{O}} \quad .$$

$$(6.1)$$

For the two adlayer structures $\Delta N_{\mathrm{Pd}} = 0$, whereas due to the reconstruction of the topmost Pd layer $\Delta N_{\mathrm{Pd}} = -1$ for the surface oxide. $\widetilde{E}^{\mathrm{bind}}_{\mathrm{O@Pd(100)}}$ is the average binding energy per oxygen atom, also including possible contributions arising from a difference in the number of surface atoms ($\Delta N_{\mathrm{Pd}} \neq 0$).

Computational Details

The different surfaces are simulated within the supercell approach using inversion symmetric slabs with 5–7 layers and 14–20 Å vacuum between subsequent slabs. The outermost 3–5 layers are fully relaxed. The muffin-tin radii are set to $R^{\mathrm{Pd}}_{\mathrm{MT}} = 2.0$ bohr for palladium and $R^{\mathrm{O}}_{\mathrm{MT}} = 1.0$ bohr for oxygen. Inside the muffin-tins the wave functions are expanded up to $l^{\mathrm{wf}}_{\mathrm{max}} = 12$ and the potential up to $l^{\mathrm{pot}}_{\mathrm{max}} = 6$. For the $p(2 \times 2)$ and $c(2 \times 2)$ structure a $[5 \times 5 \times 1]$ and for the $(\sqrt{5} \times \sqrt{5})R27°$ a $[4 \times 4 \times 1]$ MP-grid is used to integrate the BZ. Since calculations with different MP-grids are not fully comparable, the energies of the clean metal surface, $E^{\mathrm{tot}}_{\mathrm{Pd(100)}}$, and the bulk palladium, $E^{\mathrm{tot}}_{\mathrm{Pd,bulk}}$, needed to evaluate the Gibbs free energy of adsorption as defined in Eq. (6.1) are calculated in the same supercell as the corresponding adlayers or surface oxide structure. The different MP-grids of the different supercells are then chosen to provide a similar convergence of the average binding energies per oxygen atom. The energy cutoff for the expansion of the wave function in the interstitial is $E^{\mathrm{wf}}_{\mathrm{max}} = 20$ Ry and for the potential $E^{\mathrm{pot}}_{\mathrm{max}} = 196$ Ry. Using these basis set parameters the average binding energies per oxygen atom are converged within 50 meV, so that the Gibbs free energies of adsorption are converged within 1–5 meV/Å^2 (for a detailed discussion of the computational setup cf. Appendix A.2). Since the results are converged with respect to the binding energy per oxygen atom, a higher coverage induces a larger error in ΔG^{ads}. But then again, a higher coverage structure corresponds to a line with a steeper slope within the respective phase diagram, so that the x-positions of the crossing points with other lines, which determine the stability range of a certain

structure, are less sensitive to small changes in ΔG^{ads} than for low coverage structures. The total energy of the O_2 molecule is calculated by $E_{O_2}^{\text{tot}} = 2E_O^{\text{tot}} + E_{O_2}^{\text{bind}}$. The oxygen atom is calculated within a $(13 \times 14 \times 15)$ bohr supercell using only the Γ-point. The calculations are performed spin-polarized and with the same muffin-tin radius, $l_{\text{max}}^{\text{wf}}$, $l_{\text{max}}^{\text{pot}}$, $E_{\text{max}}^{\text{pot}}$, and $E_{\text{max}}^{\text{wf}}$ as above.

To determine the binding energy of the oxygen molecule, $E_{O_2}^{\text{bind}}$, the muffin tin radius for the oxygen in the O_2 molecule and O atom is set to $R_{\text{MT}}^{O} = 1.1$ bohr. The calculations are performed in a $(13 \times 14 \times 18)$ bohr supercell for the molecule, resp. a $(13 \times 14 \times 15)$ bohr supercell for the atom, using again only the Γ-point. Both, the atom and the molecule are treated spin-polarized. $l_{\text{max}}^{\text{wf}}$, $l_{\text{max}}^{\text{pot}}$, and $E_{\text{max}}^{\text{pot}}$ are chosen as above, the energy cutoff for the expansion of the wave function in the interstitial is increased up to $E_{\text{max}}^{\text{wf}} = 37$ Ry. The bond length in the O_2 molecule is fully optimized for each exchange-correlation functional. Within this highly converged basis set the binding energy of the O_2 molecule is calculated as $E_{O_2}^{\text{bind}} = -6.20$ eV (PBE), -5.75 eV (RPBE) and -7.56 eV (LDA) (for a detailed discussion cf. Appendix A.3).

Surface Phase Diagrams

The binding energies and the corresponding Gibbs free energies of adsorption of the different structures are listed in Tab. 6.3 for the PBE, the RPBE and the LDA as approximation to the exchange-correlation functional. The dependence of the Gibbs free energy of adsorption on the chemical potential of the oxygen gas phase is visualized in Fig. 6.5, using the PBE results. Focussing first on the left graph in Fig. 6.5, there are five different lines for the clean Pd(100) surface, the $p(2 \times 2)$, the $c(2 \times 2)$, the $(\sqrt{5} \times \sqrt{5})R27°$ structure and for the PdO bulk with increasing slope corresponding to the increasing oxygen coverage from 0.0 ML (clean) to 0.8 ML $((\sqrt{5} \times \sqrt{5})R27°)$ and finally a vertical line indicating the stability region of the bulk oxide (*infinite* number of oxygen atoms). As explained in detail in Section 4.3 the thermodynamically most stable structure is always the one that maximizes ΔG^{ads}. Since the y-axis in the left plot of Fig. 6.5 is inverted this thermodynamically most stable structure will be the one with the *lowest* line. It should be noted that at finite temperatures the transition between the different phases will not be sharp, but due to contributions from the configurational entropy coexistence regions will develop, containing a mixture of energetically neighboring structures.

Starting at a very low oxygen chemical potential the clean Pd(100) surface has to be the most stable phase. At $\Delta\mu_O = -1.35$ eV the line of the $p(2 \times 2)$ structure crosses the zero line and the $p(2 \times 2)$ is the most stable phase. With further increasing $\Delta\mu_O$ the $(\sqrt{5} \times \sqrt{5})R27°$ surface oxide becomes stable $(\Delta\mu_O = -1.15$ eV$)$ and finally the stability region of the bulk oxide is reached $(\Delta\mu_O = -0.87$ eV$)$, which is determined by the heat of formation of PdO. The PBE value for the heat of formation of PdO in the low temperature limit, $\Delta G^f(T = 0\,\text{K}, p = 0) = -0.87$ eV, compares rather well with the experimental value of $\Delta G_{\text{exp}}^f(T \to 0\,\text{K}, p = 1\,\text{atm}) = -0.97$ eV [11]. For the top two x-axes of the left graph in Fig.6.5 the chemical potential has been converted

		$p(2 \times 2)$	$c(2 \times 2)$	$(\sqrt{5} \times \sqrt{5})R27°$
PBE	$\widetilde{E}^{\mathrm{bind}}$	-1.35	-1.10	-1.20
	$\Delta G^{\mathrm{ads}}(\Delta\mu_O = 0)$	-43.20	-70.33	-123.35
RPBE	$\widetilde{E}^{\mathrm{bind}}$	-0.98	-0.77	-0.92
	$\Delta G^{\mathrm{ads}}(\Delta\mu_O = 0)$	-30.84	-48.66	-92.96
LDA	$\widetilde{E}^{\mathrm{bind}}$	-2.15	-1.79	-1.77
	$\Delta G^{\mathrm{ads}}(\Delta\mu_O = 0)$	-73.06	-121.76	-192.46

Table 6.3: Average binding energy per oxygen atom in eV and Gibbs free energy of adsorption in meV/Å^2 for $\Delta\mu_O = 0$ for the two adlayers and the surface oxide on Pd(100). The different values obtained using the PBE, the RPBE and the LDA as approximation to the exchange correlation functional are listed.
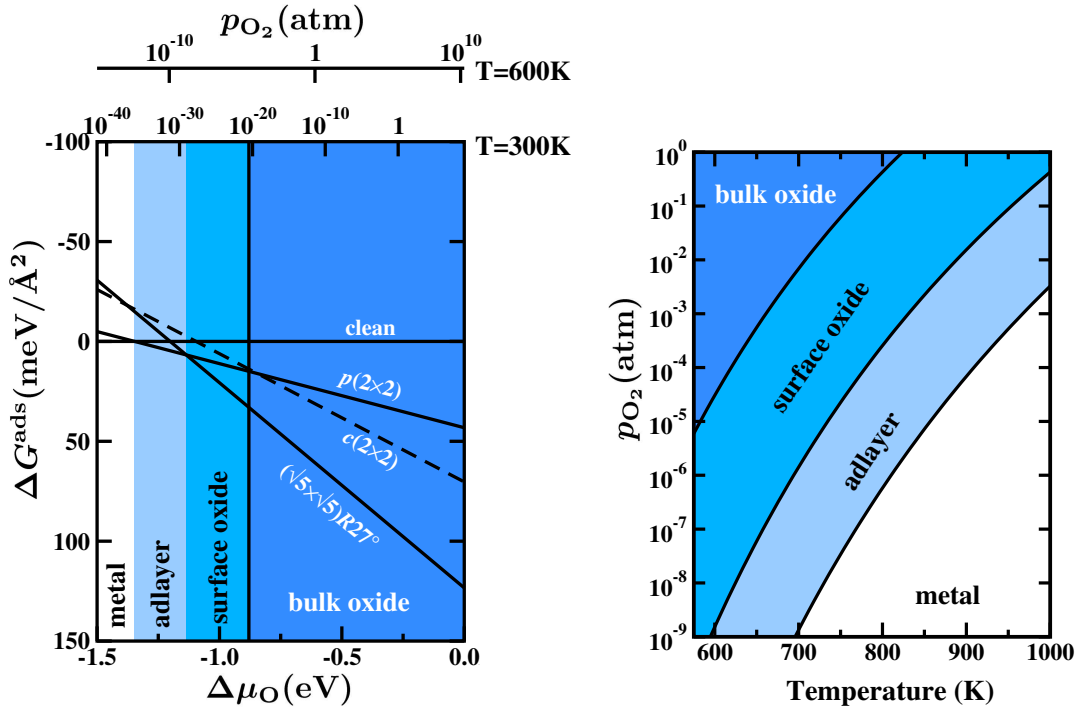

Figure 6.5: Surface phase diagram of Pd(100) in thermodynamic equilibrium with an oxygen gas phase using the DFT-PBE results. In the left graph the Gibbs free energy of adsorption is plotted vs. the oxygen chemical potential. In the right graph the $\Delta\mu_O$ values marking the stability regions for every phase are converted into the respective (T, p)-conditions, showing the thermodynamically most stable phase at any given T and p.

$E_{\rm xc}$	metal $\rightarrow p(2 \times 2)$	$p(2 \times 2) \rightarrow (\sqrt{5} \times \sqrt{5})R27°$	$(\sqrt{5} \times \sqrt{5})R27° \rightarrow$ PdO bulk
PBE	-1.35	-1.15	-0.87
RPBE	-0.98	-0.90	-0.62
LDA	-2.15	-1.64	-1.42

Table 6.4: Values of the oxygen chemical potential $\Delta\mu_{\rm O}$ in eV for the phase boundaries between the different oxidation phases of the Pd(100) surface obtained using the PBE, RPBE and LDA exchange-correlation functional.

into pressures scales at two fixed temperatures (cf. Section 4.4), which can provide a more intuitive understanding of this figure. An even more intuitive representation of the stability of the different phases is shown in the right plot of Fig. 6.5. Here, the one-dimensional dependence on the chemical potential is transferred into a two-dimensional dependence on temperature and pressure. The plot then only shows the most stable structures in the corresponding (T, p)-range. At high temperatures and low pressures the clean metal surface is stable, lowering the temperature or increasing the pressure corresponds to an increase in the oxygen chemical potential and thus results again in a stabilization of the oxygen containing structures.

In Fig. 6.5 it can be seen, that the $c(2 \times 2)$ structure observed in ultra high vacuum (UHV) experiments does not appear to be thermodynamically stable under any oxygen gas phase conditions. Thus, the $c(2 \times 2)$ phase is most likely a meta-stable state produced by the exposure kinetics. On the other hand, the $p(2 \times 2)$ and the $(\sqrt{5} \times \sqrt{5})R27°$ structure are both stable over an extended (T, p)-range. The stability of the surface oxide structure notably exceeds the one of the bulk oxide, so that the surface oxide can actually be considered as a separate phase, which might exhibit properties different from a simple adlayer structure as well as from the bulk oxide phase.

To investigate the influence of the chosen exchange-correlation functional on the obtained results, the surface phase diagram is also calculated using the RPBE and LDA (cf. Tab. 6.3). The results for all three exchange-correlation functionals are shown in Fig. 6.6 together with experimental results obtained by surface x-ray diffraction (SXRD) measurements [23]. Focussing first on the three theoretical plots it becomes obvious, that there is a significant shift in the phase boundaries for the different functionals (cf. Tab. 6.4). Nevertheless, all three functionals show the same phases and the same ordering of phases with respect to the (T, p)-conditions. The $c(2 \times 2)$ phase does not appear in any of the phase diagrams and the surface oxide is stable over a wide (T, p)-range independent of the functional used.

Comparing the theoretical phase diagrams to the experimental one (lower right plot in Fig 6.6), it can be seen, that also in the SXRD measurements the $c(2 \times 2)$ structure is not observed. Concentrating on the experimental and PBE results, the two phase diagrams actually show a quite good agreement over a wide range of environmental conditions. Especially the transition from the metal to the $p(2 \times 2)$ to the $(\sqrt{5} \times \sqrt{5})R27°$ in going form high temperatures and low pressures to lower T and
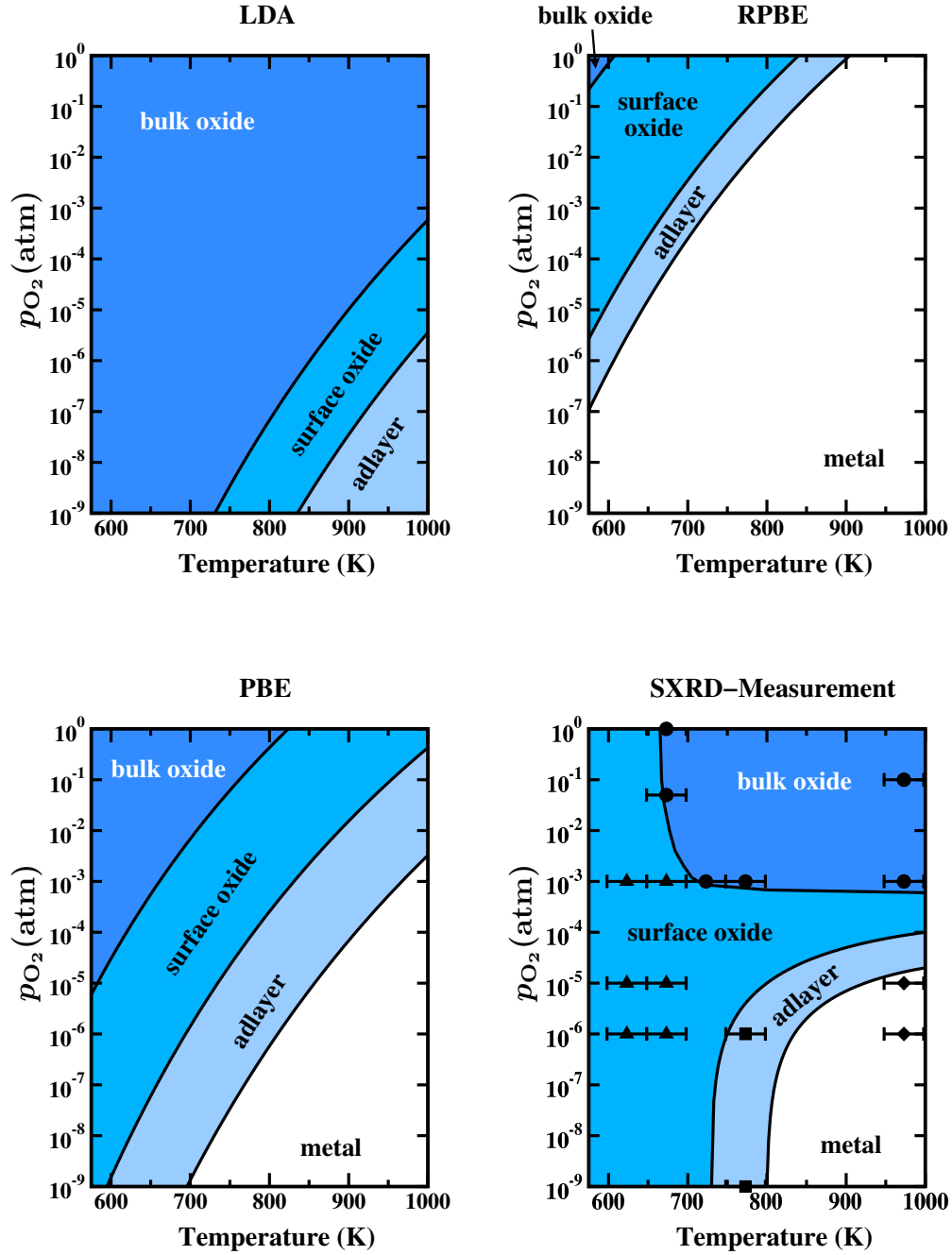
Figure 6.6: Surface phase diagrams for the Pd(100) surface in equilibrium with an oxygen gas phase for the LDA, RPBE and PBE exchange-correlation functional. The lower right figure shows experimental results obtained by surface x-ray diffraction (SXRD) measurements [23].

higher p is rather well reproduced. There is, however, one noticeable difference, which can not be explained by the uncertainties underlying the atomistic thermodynamics approach as well as the experimental setup. In the upper left corner of the experimental phase diagram (low temperatures, high pressure) the $(\sqrt{5} \times \sqrt{5})R27°$ surface oxide is observed. Since the atomistic thermodynamics approach, which assumes full thermodynamic equilibrium of all phases, predicts the bulk oxide to be stable under such (T, p)-conditions, this can be interpreted as a kinetic limitation to the growth of the bulk oxide. Even without the theoretical phase diagrams, this interpretation is still consistent. In thermodynamic equilibrium the different phases are separated by lines of constant chemical potential, which have to be always parallel to the ones shown in the theoretical phase diagrams. The phase boundary between the surface oxide and the bulk oxide in the experimental phase diagram is certainly not parallel to such a line of constant $\Delta\mu_O$, which confirms the assumption that the formation of the bulk oxide is hindered by kinetic effects on the time scale accessible to the SXRD experiments.

Evaluating The Gibbs Free Energy

The discussed theoretical phase diagrams are based on DFT total energies only, neglecting all other contributions to the Gibbs free energy. The uncertainty in the presented results introduced by such a simplification can be examined by an order of magnitude estimate of the different contributions to ΔG^{ads} besides the total energy, as discussed in Section 4.3.1. If this first approximation reveals, that the drawn physical conclusions are significantly changed by considering all contributions to ΔG^{ads}, the respective terms have to be calculated explicitly. However, the order of magnitude estimate can already be obtained with much less computational effort and is thus very helpful to decide, whether or not it is necessary to evaluate the entire Gibbs free energy.

For the here investigated structures the contributions arising from the pV-term as well as from the configurational entropy will be in the same range as for the general case discussed in Section 4.3.1, i.e. the two terms will only contribute less than $3\,\text{meV}/\text{Å}^2$ to the Gibbs free energy, which will not significantly influence the results shown here (cf. Fig. 6.5).

The vibrational contribution, though, can be somewhat larger and will vary for every considered structure. Following the approach outlined in Section 4.2 the vibrational contribution to the Gibbs free energy of adsorption of the $p(2 \times 2)$ phase is approximately given by

$$\Delta G^{\text{ads,vib}}(T) \approx -\frac{1}{A}\left(F^{\text{vib}}(T, \bar{\omega}^{\text{surf}}_{\text{O−Pd}}) - \frac{1}{2}F^{\text{vib,ZPVE}}(\bar{\omega}^{\text{gas}}_{\text{O}_2})\right) \quad , \qquad (6.2)$$

where $\bar{\omega}^{\text{surf}}_{\text{O−Pd}}$ is the averaged Einstein frequency of an oxygen atom adsorbed in a fourfold hollow site on the Pd(100) surface. Here, the change in the vibrational contribution of the Pd atoms in the clean and the adlayer structure is neglected, so that
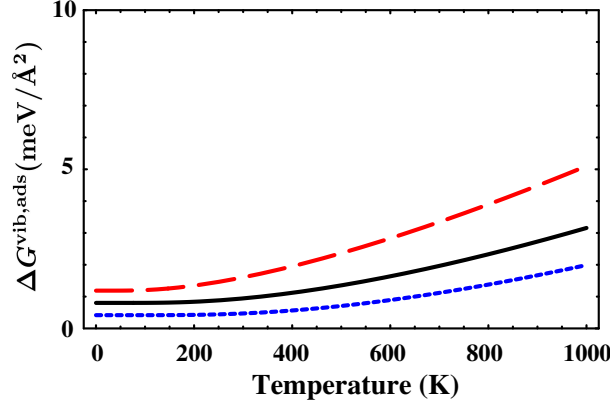
Figure 6.7: Vibrational contribution to the Gibbs free energy of adsorption for the $p(2 \times 2)$ adlayer on Pd(100) within a simple Einstein-approximation (see text).

the vibrational contribution to ΔG^{ads} is approximated by the change in the vibrational energy of the oxygen molecule in the gas phase and the oxygen atom adsorbed on the surface. For the oxygen molecule only the zero-point vibration energy (ZPVE, not included in the presented DFT total energies) has to be considered, since the (T, p)-dependent contributions are already summarized in $\Delta\mu_{\text{O}}$. Assuming a characteristic frequency of $\bar{\omega}_{\text{O}-\text{Pd}}^{\text{surf}} = 48\,\text{meV}$ for the Pd-O stretch frequency [116] of the adsorbed oxygen and $\bar{\omega}_{\text{O}_2}^{\text{gas}} = 196\,\text{meV}$ for the O-O vibration in the gas phase [117] the vibrational contribution to ΔG^{ads} for the $p(2 \times 2)$ stays below $\sim 3\,\text{meV}/\text{Å}^2$ for temperatures up to 1000 K (cf. black line in Fig. 6.7). Even if the characteristic frequency of the Pd-O stretching frequency is changed by $\pm 50\,\%$ (red-dashed, $-50\,\%$, blue-dotted, $+50\,\%$, lines in Fig. 6.7) the contribution does not increase considerably.

For the $c(2 \times 2)$ phase this contribution simply doubles, since there are two oxygen atoms in the (2×2) surface unit cell. But still for the temperature range considered here, which is up to 600 K, this only leads to a maximum estimated contribution of $\sim 6\,\text{meV}/\text{Å}^2$, which would not lead to an appearance of the $c(2 \times 2)$ structure as a thermodynamically stable phase.

Considering the surface oxide structure an additional contribution arising from the change in the vibrational energy between bulk and surface Pd atoms has to be taken into account, since the $(\sqrt{5} \times \sqrt{5})R27°$ structure contains one surface atom less then the corresponding Pd(100) surface, which has to be balanced by the bulk reservoir ($\Delta N_{\text{Pd}} = -1$). The vibrational contribution to ΔG^{ads} for the surface oxide structure can then be estimated by

$$\Delta G^{\text{ads,vib}}(T) \approx -\frac{1}{A}\left(4F^{\text{vib}}(T, \bar{\omega}_{\text{O}-\text{Pd}}^{\text{surf}}) - \frac{4}{2}F^{\text{vib,ZPVE}}(\bar{\omega}_{\text{O}_2}^{\text{gas}})\right)$$
$$-\frac{3}{A}\left(F^{\text{vib}}(T, \bar{\omega}_{\text{Pd}}^{\text{bulk}}) - F^{\text{vib}}(T, \bar{\omega}_{\text{Pd}}^{\text{surf}})\right) \quad . \tag{6.3}$$

72

Using a characteristic frequency of $\bar{\omega}_{\mathrm{Pd}}^{\mathrm{bulk}} = 20\,\mathrm{meV}$ for bulk Pd [118] and allowing a $\pm 50\,\%$ change for the surface atoms this contribution will again be below $\sim 6\,\mathrm{meV/\mathring{A}^2}$ for temperatures up to $600\,\mathrm{K}$. Allowing also for an uncertainty of $\pm 50\,\%$ in the characteristic frequencies of the bulk Pd and the adsorbed oxygen will slightly change this contribution, but it will still be below $\sim 10\,\mathrm{meV/\mathring{A}^2}$ for all temperatures up to $600\,\mathrm{K}$. However, even if the Gibbs free energy of the adsorption of the surface oxide is changed by $\pm 10\,\mathrm{meV/\mathring{A}^2}$, the surface oxide will still be a thermodynamically stable phase over an extended (T, p)-range, which is one of the important conclusions of this study.

The previous discussion shows, that the uncertainty arising from approximating the Gibbs free energy by the leading total energy term only does not significantly affect any of the above drawn conclusions. Regarding the absolute values of ΔG^{ads} and the resulting phase boundaries, the uncertainty introduced by the choice of the exchange-correlation functional is in any case much larger than any error introduced by not considering all contributions to ΔG^{ads}. Thus, an explicit evaluation of all terms included in ΔG^{ads} does not appear to be necessary in this case.

6.3   PdO Low-Index Surfaces

Despite the different stages involved in the oxidation of the Pd(100) surface, in an oxygen rich atmosphere the formation bulk oxide is usually observed as the final stage. Experimentally, a roughening of the surface is found along with the formation of PdO [23, 113]. This suggests that the bulk oxide growth does not proceed via a thickening of the PdO(101) template provided by the $(\sqrt{5} \times \sqrt{5})R27°$ surface oxide, but instead 3-dimensional PdO nanoparticles are formed through faceting. The facets of such a nanoparticle will be built up by different PdO surface structures.

To obtain a first insight into the morphology of PdO crystals, the structure and stability of different PdO surfaces in equilibrium with an oxygen gas phase are discussed in this Section. Since there is as good as no experimental information about the atomic structure and composition of crystalline PdO surfaces, the discussion is limited to all possible (1×1) terminations of the low-index surfaces of PdO. An investigation of possible surface reconstructions is hardly feasible without any information about the surface composition and periodicity. Nevertheless, with the knowledge of the surface energetics it is then possible to determine a first approximation to the equilibrium shape of a single crystal by setting up a so-called Wulff construction within the compiled data set.

6.3.1   Structure And Stability

Due to the tetragonal structure of the PdO unit cell (cf. Fig. 6.4) there are five inequivalent low-index surface orientations as illustrated in Fig. 6.8. Each of these surface orientations exhibits 2–3 different (1×1) surface terminations depending on at
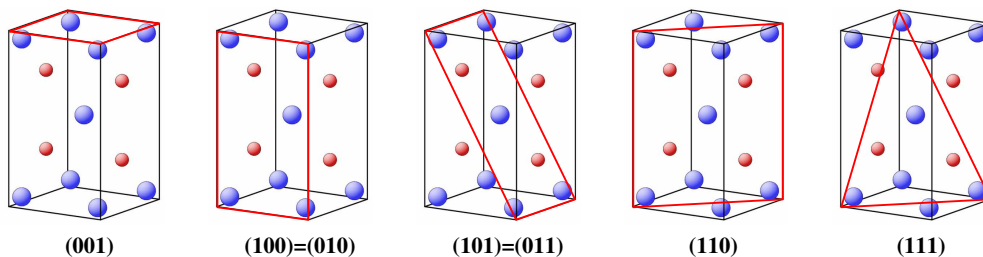
Figure 6.8: Schematic illustration of the low-index PdO surfaces. The respective planes are indicated by the red lines. Small red spheres represent oxygen atoms, large blue ones palladium atoms.

which layer the bulk-stacking sequence is truncated at the surface. For the PdO(001) surface, parallel to the xy-plane, there are two different surface terminations, one with only Pd atoms [PdO(001)-Pd] and one with only O atoms [PdO(001)-O] in the topmost layer. A schematic illustration of all discussed surface terminations is shown as inset in Fig. 6.9 – Fig. 6.11. The PdO(100) surface (parallel to the yz-plane), which is equivalent to the PdO(010) surface (parallel to the xz-plane), shows also two different terminations, one again containing only Pd atoms in the topmost layer [PdO(100)-Pd] and the other Pd as well as O atoms [PdO(100)-PdO]. The PdO(101) orientation, which is equivalent to the PdO(011) orientation, exhibits an O-Pd$_2$-O trilayer stacking structure. For this orientation there exist three different terminations. For the stoichiometric termination the layer stacking is truncated just between two consecutive O-Pd$_2$-O trilayers [PdO(101)]. The other two terminate either after the Pd layer [PdO(101)-Pd] or after the second O layer [PdO(101)-O], yielding two O layers at the top. The remaining two orientations, PdO(110) and PdO(111), are both characterized by alternating layers of Pd and O atoms along the surface normal. Thus, there are two possible terminations for each orientation, one having just Pd atoms [PdO(110)-Pd and PdO(111)-Pd] and the other having only O atoms in the topmost layer [PdO(110)-O and PdO(111)-O].

Out of these 11 different (1×1) terminations only one is stoichiometric, the PdO(101) termination, whereas the other 10 exhibit either an excess of oxygen or palladium atoms. These 10 surface terminations would therefore be considered as so-called *polar* surfaces, which from an electrostatic point of view were traditionally thought to be rather unstable [119, 120]. Theoretically, the stability of polar oxide surfaces has been predicted for several cases, e.g. for different iron oxide surfaces as well as for RuO$_2$ surfaces terminations [74, 76, 121]. A possible connection between the stability and the polarity of the different PdO surface terminations is discussed in Section 6.3.3.

To compare the stability of the different surface structures in thermodynamic equilibrium with the surrounding oxygen gas phase the atomistic thermodynamics approach is used as discussed in Section 4.2. For palladium oxide the surface free energy in the oxygen poor limit ($\Delta\mu_O = \Delta G^f_{PdO}$, i.e. now a range of $\Delta\mu_O$ beyond the one

shown in Fig. 6.5 and Fig. 6.6 is discussed) is given by

$$\gamma_{\mathrm{O-poor}} \approx \frac{1}{A}\left[E_{\mathrm{PdO}}^{\mathrm{surf}}(N_{\mathrm{Pd}}, N_{\mathrm{O}}) - N_{\mathrm{O}}E_{\mathrm{PdO}}^{\mathrm{bulk}} - \left(N_{\mathrm{Pd}} - N_{\mathrm{O}}\right)E_{\mathrm{Pd}}^{\mathrm{bulk}}\right] \quad . \qquad (6.4)$$

Correspondingly, the surface free energy in the oxygen rich limit ($\Delta\mu_{\mathrm{O}} = 0$) is

$$\gamma_{\mathrm{O-rich}} = \gamma_{\mathrm{O-poor}} + \frac{1}{A}\left(N_{\mathrm{O}} - N_{\mathrm{Pd}}\right)\Delta G_{\mathrm{PdO}}^{f}(T = 0\,\mathrm{K}, p = 0) \quad . \qquad (6.5)$$

Again, the Gibbs free energies have been approximated by the total energies in a first step. Following the discussion in Section 4.2 the contribution from the pV-term as well as from the configurational entropy to the Gibbs free energy can be estimated as below $3\,\mathrm{meV/\mathring{A}^2}$. To obtain an order of magnitude estimate of the vibrational contribution to the surface free energy the Einstein approximation to the phonon DOS can be employed as explained in Section 4.2. Experimental results are used to estimate the characteristic frequencies of palladium and oxygen in PdO bulk with $\bar{\omega}_{\mathrm{Pd}}^{\mathrm{bulk}} = 20\,\mathrm{meV}$ and $\bar{\omega}_{\mathrm{O}}^{\mathrm{bulk}} = 70\,\mathrm{meV}$ [81]. To now evaluate Eq. (4.28) the number of Pd and O atoms at the surface has to be identified for every surface termination. An atom is considered to be *at* the surface, if its nearest neighbor coordination is changed compared to the coordination in the bulk structure, i.e. in the case of the PdO(101) termination one Pd and one O atom would be counted as surface atoms, whereas e.g. for the PdO(001)-Pd termination only the topmost Pd layer is considered as surface atoms. Within this approximation the vibrational contribution to the surface free energy stays within a range of about 10–$20\,\mathrm{meV/\mathring{A}^2}$ for all temperatures up to $T = 600\,\mathrm{K}$ and for all considered PdO terminations. This is certainly not a very small contribution, but in the discussion of the results it will become apparent below that even a 10–$20\,\mathrm{meV/\mathring{A}^2}$ change in the surface free energies will not affect the conclusions drawn.

Computational Details

To simulate the different PdO surfaces the supercell approach is applied using symmetric slabs with 7–11 layers and a 12–$15\,\mathring{A}$ vacuum between subsequent slabs. The outermost 2–4 layers are fully relaxed for all surfaces. Within this setup of the supercells the absolute surface energies are converged within $3\,\mathrm{meV/\mathring{A}^2}$. The muffin tin radii for palladium and oxygen are set to $R_{\mathrm{MT}}^{\mathrm{Pd}} = 1.8\,\mathrm{bohr}$ and $R_{\mathrm{MT}}^{\mathrm{O}} = 1.3\,\mathrm{bohr}$. The wave function expansion inside the muffin tins is considered up to $l_{\mathrm{max}}^{\mathrm{wf}} = 12$ and the potential expansion up to $l_{\mathrm{max}}^{\mathrm{pot}} = 6$. The BZ-integration is performed using MP grids. The MP grids and number of **k**-points in the irreducible part of the BZ are listed in Tab. 6.5. The energy cutoff for the planewave representation in the interstitial region is $E_{\mathrm{max}}^{\mathrm{wf}} = 17\,\mathrm{Ry}$ for the wave function and $E_{\mathrm{max}}^{\mathrm{pot}} = 196\,\mathrm{Ry}$ for the potential. With these basis sets the absolute surface energies of the different PdO surfaces are converged within 1–$2\,\mathrm{meV/\mathring{A}^2}$ regarding the **k**-points and 3–$4\,\mathrm{meV/\mathring{A}^2}$ regarding the planewave cutoff in the interstitial $E_{\mathrm{max}}^{\mathrm{wf}}$. Errors in the relative energies

PdO surface	MP grid	no. of irred. **k**-points
$(100) \equiv (010)$	$[3 \times 7 \times 1]$	8
(001)	$[7 \times 7 \times 1]$	16
$(101) \equiv (011)$	$[1 \times 3 \times 7]$	8
(110)	$[4 \times 3 \times 1]$	6
(111)	$[2 \times 4 \times 1]$	6

Table 6.5: Employed Monkhorst-Pack grids and corresponding number of **k**-points in the irreducible part of the Brillouin zone for the different (1×1) surface unit cells of the low-index PdO surfaces.

comparing different surfaces terminations are even smaller (for a detailed discussion of the computational setup cf. Appendix A.1).

Surface Free Energy

In Fig. 6.9 – Fig. 6.11 the surface free energy plots of all eleven (1×1) terminations are shown. As expected from the general discussion in Section 4.2 terminations with an oxygen excess show a negative slope, i.e. they become more stable in a more oxygen-rich gas phase, whereas terminations with an oxygen deficiency and a positive slope become less stable with increasing oxygen chemical potential. The vertical dotted lines mark the stability range of the oxide surfaces (cf. Section 4.2), determined by the heat of formation of PdO, $\Delta G^f_{\mathrm{PdO}}(T = 0\,\mathrm{K}, p = 0) = -0.87\,\mathrm{eV}$ (PBE). To take into account the uncertainty in these theoretically well defined but computational only approximate limits, the x-axes of the surface free energy plots are somewhat extended outside these boundaries.

Comparing the five plots for the different surface orientations in Fig. 6.9 – Fig. 6.11 the very low surface energy, i.e. high stability, of the PdO(100)-PdO termination is clearly observable. Only the PdO(101) and towards the O-rich limit the PdO(110)-O and the PdO(111)-O surfaces exhibit a comparably low surface free energy. All other terminations show a rather high surface free energy over the whole range of $\Delta\mu_{\mathrm{O}}$, especially all those terminations with Pd atoms in the outermost layer. Considering the energy scale of the surface free energy plots it can be noted, that the uncertainty of 10–$20\,\mathrm{meV/\AA^2}$ in γ introduced by neglecting the vibrational contributions to the Gibbs free energies does not affect the ordering of the different surface terminations with respect to their thermodynamic stability.

To obtain an estimate for the uncertainty introduced by the choice of the PBE as approximation to the exchange-correlation functional all surface free energies are also calculated within the LDA. To set up the supercells for these LDA calculations the respective optimized lattice constants for PdO bulk are used (cf. Tab. 6.2). The surface free energies of all 11 surface terminations in the oxygen-poor limit obtained within the PBE and LDA are listed in Tab. 6.6. Comparing the values for $\gamma_{\mathrm{O\text{-}poor}}$
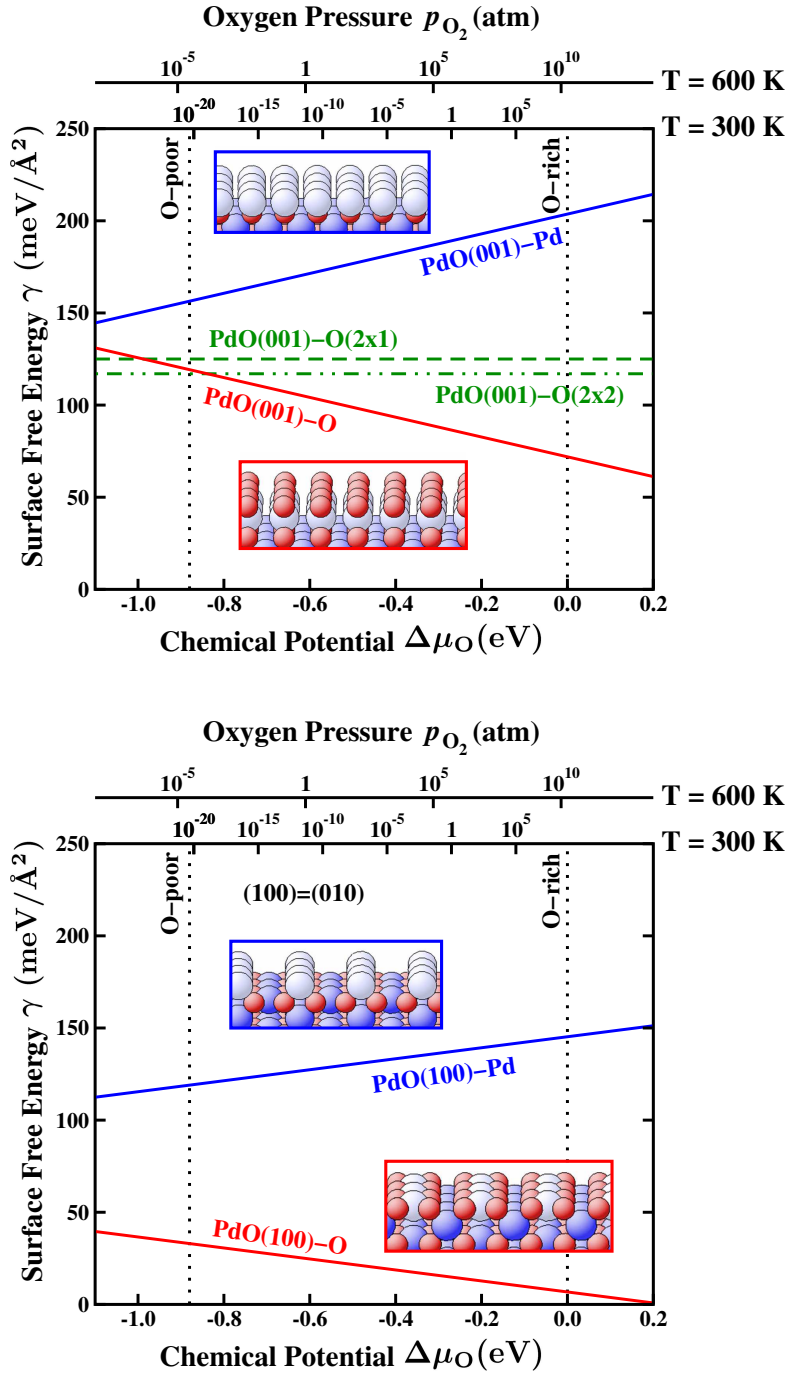
Figure 6.9: Surface free energies for the PdO(001) and PdO(100) surfaces. Solid lines indicate (1×1) terminations and dashed lines larger unit cell reconstructions. The vertical dotted lines specify the range of $\Delta\mu_O$. In the top two x-axes the dependence on the oxygen chemical potential has been converted into pressure scales at $T = 300\,K$ and $600\,K$. The insets show the surface geometries of the corresponding (1×1) terminations, where the small red spheres illustrated O atoms and large blue spheres Pd atoms. In the upper graph, additionally shown are the lines of two reconstructions discussed in Section 6.3.3.

Figure 6.10: Surface free energies for the PdO(101) and PdO(110) surfaces. Solid lines indicate (1×1) terminations and dashed lines larger unit cell reconstructions. The vertical dotted lines specify the range of $\Delta\mu_O$. In the top two x-axes the dependence on the oxygen chemical potential has been converted into pressure scales at $T = 300\,\text{K}$ and $600\,\text{K}$. The insets show the surface geometries of the corresponding (1×1) terminations, where the small red spheres illustrated O atoms and large blue spheres Pd atoms. In the lower graph, additionally shown are the lines of two reconstructions discussed in Section 6.3.3.
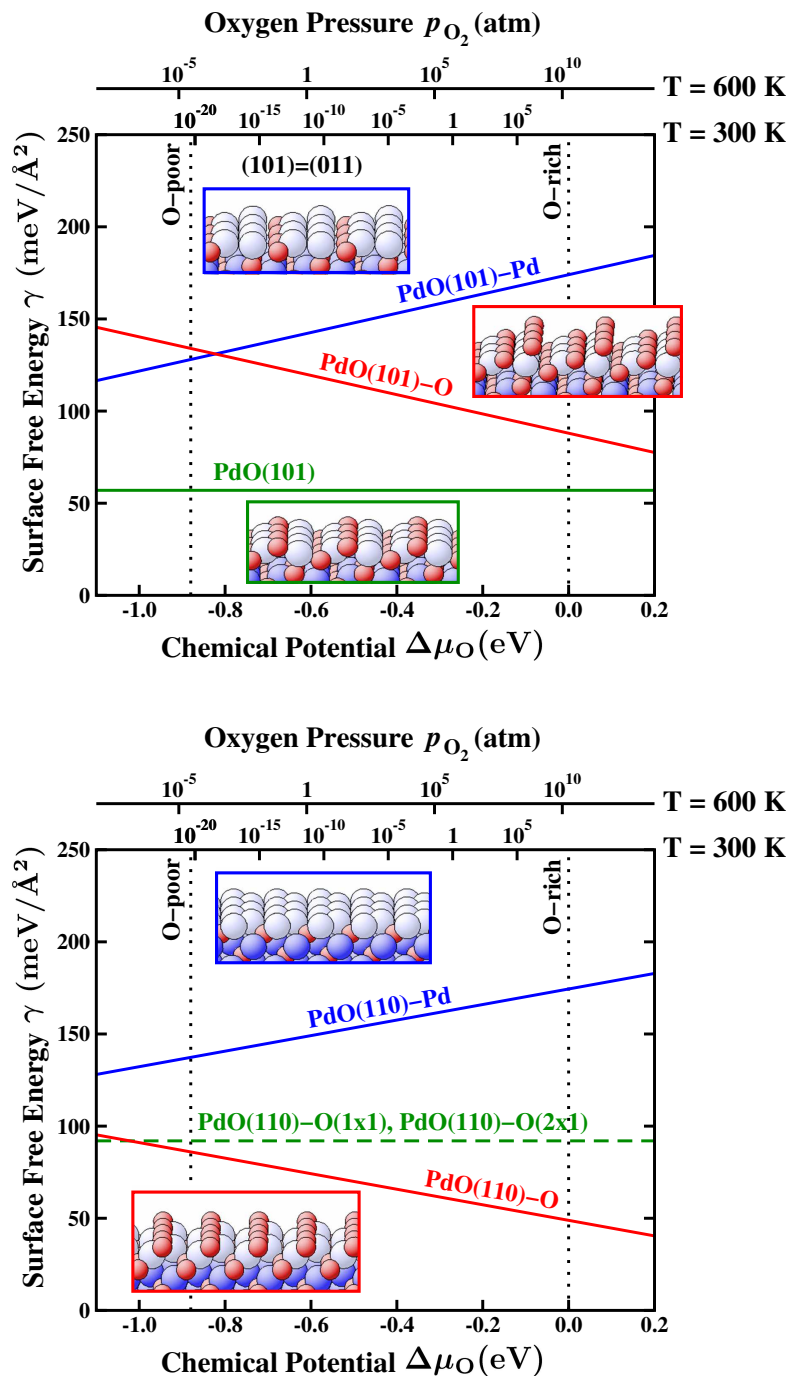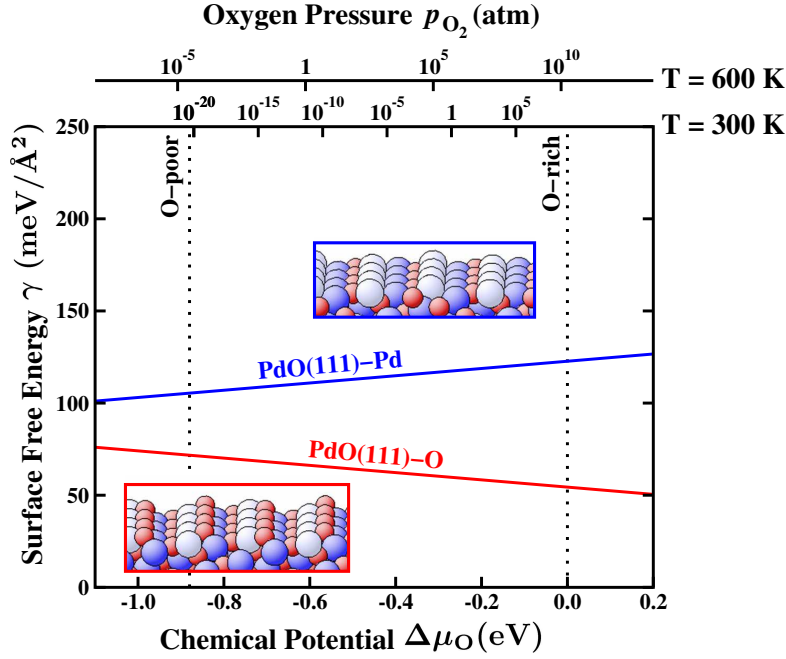
Figure 6.11: Surface free energies for the PdO(111) surface. Solid lines indicate (1×1) terminations. The vertical dotted lines specify the range of $\Delta\mu_O$. In the top two x-axes the dependence on the oxygen chemical potential has been converted into pressure scales at $T = 300\,\text{K}$ and $600\,\text{K}$. The insets show the surface geometries of the corresponding (1×1) terminations, where the small red spheres illustrated O atoms and large blue spheres Pd atoms.

calculated using these two different exchange-correlation functionals it can be observed that the absolute values of the LDA surface energies are $30–50\,\text{meV/Å}^2$ higher than the PBE surface energies. Focussing however on the relative differences between the different surface terminations the two approaches agree within $10–30\,\text{meV/Å}^2$. These relative energetic differences with respect to the PdO(100)-PdO termination, which is the lowest energy surface in both the LDA and PBE approach, are also indicated in Tab. 6.6. The energetic ordering does not seem to depend very much on the choice of the exchange-correlation functional, and since only these relative energy differences are decisive in determining the equilibrium shape of a single crystal, the DFT accuracy is expected to be rather high for this specific quantity.

Surface termination	$\gamma_{\text{O-poor}}$ PBE		$\gamma_{\text{O-poor}}$ LDA	
PdO(100)-PdO	33	(0)	59	(0)
PdO(100)-Pd	119	(+86)	170	(+111)
PdO(001)-O	119	(+86)	162	(+103)
PdO(001)-Pd	156	(+123)	212	(+153)
PdO(101)	57	(+24)	86	(+27)
PdO(101)-O	134	(+101)	180	(+121)
PdO(101)-Pd	128	(+95)	173	(+114)
PdO(110)-O	86	(+53)	119	(+60)
PdO(110)-Pd	137	(+104)	173	(+114)
PdO(111)-O	72	(+39)	109	(+50)
PdO(111)-Pd	105	(+72)	143	(+84)

Table 6.6: Surface free energies of all low-index PdO (1×1) terminations at the oxygen-poor limit, as calculated within the GGA-PBE and the LDA. All energies are in meV/Å^2, and the numbers in brackets denote the energetic difference with respect to the lowest-energy PdO(100)-PdO termination.

6.3.2   Wulff Construction

With the results obtained for the surface free energies of the different (1×1) PdO terminations a Wulff construction [122] for a PdO single crystal is set up. The Wulff construction gives the shape of a single crystal in its thermodynamic equilibrium, providing a (simple) graphical method to find the shape with the lowest free energy. For this construction vectors normal to all crystallographic faces are drawn originating from one arbitrary point. On each vector a mark is placed at a distance from the center point, that is proportional to the corresponding surface energy. Through this mark a plane normal to the vector is constructed, i.e. planes belonging to a termination with a low surface energy are closer to the center than planes of high surface energy terminations. The intersecting planes result in a closed polyhedron, which then yields the equilibrium crystal shape.

Since here only the afore discussed eleven (1×1) terminations are considered, the resulting *constrained* Wulff construction is more intended to compare and evaluate the relative energies of the different surface orientations rather than to actually quantitatively predict the equilibrium PdO crystallite shape. To generate a complete Wulff construction possible surface reconstructions would have to be taken into account, which might significantly influence the theoretical equilibrium shape of a crystal.

Since the surface free energy of each termination exhibits a different dependence on the chemical potential of the surrounding oxygen gas phase, also the resulting Wulff constructions will vary with $\Delta\mu_{\mathrm{O}}$. Thus, in Fig. 6.12 the obtained Wulff polyhedra are presented for the two extreme environmental conditions, i.e. for very low oxygen chemical potential (the O-poor limit) and for high oxygen chemical potential (the O-rich limit). Due to the tetragonal symmetry of the PdO unit cell (cf. Fig. 6.4) the polyhedra must be symmetric with respect to the xy-plane. Therefore in Fig. 6.12 only the upper half of each polyhedron is shown, and the beginning of the lower half is only indicated by the light-red part.

As already expected from comparing the values of the surface free energies, the PdO(100)-PdO termination forms largely dominating facets (red, rectangular facets in Fig. 6.12) in both the O-rich and O-poor limit. The other triangular, blue facets correspond to the stoichiometric PdO(101) termination. All other investigated surface terminations do not contribute to the Wulff construction, since their surface free energies are so high, that the resulting planes lie completely outside of the shown polyhedra and do not cross them at any point. The two polyhedra in Fig. 6.12 are scaled in such a way, that the area of the PdO(101) facets is equal in the O-poor and O-rich limit, since also the surface energy of this termination is constant with respect to the oxygen chemical potential. Correspondingly, the area of the PdO(100)-PdO facets in the Wulff construction increases strongly in going from the oxygen-poor to the oxygen-rich limit as the surface energy of this termination decreases. Already in the O-poor limit the PdO(100)-PdO termination forms 72 % of the whole area of the polyhedron. In the O-rich limit the fraction covered by PdO(100)-PdO facets rises up to 94 %. If the Wulff construction is set up using the surface free energies
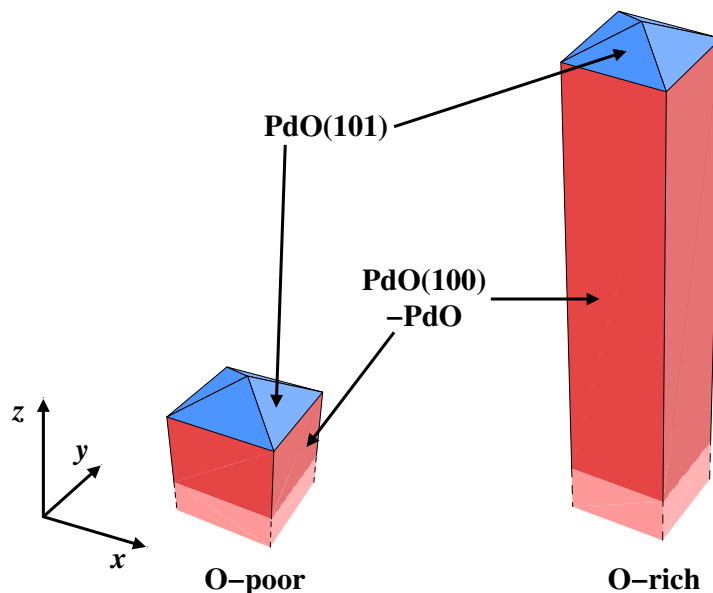
Figure 6.12: Constrained Wulff construction at the oxygen-poor (left) and oxygen-rich (right) limits. The construction is constrained to the investigated (1×1) terminations. The two polyhedra are symmetric with respect to the xy-plane and only the upper half is shown correspondingly. The red planes correspond to the PdO(100)-PdO, the blue ones to the PdO(101) termination.

obtained within the LDA-DFT approach, the resulting polyhedra exhibit the same facets as the ones obtained with the PBE exchange-correlation functional, i.e. only the PdO(100)-PdO and PdO(101) terminations contribute to the shape. Again the PdO(100)-PdO facets are the prevailing ones covering $66\,\%$ of the surface area in the O-poor limit and $82\,\%$ in the O-rich limit. The good agreement of the PBE and LDA results supports the previous assumption, that although the absolute surface free energies depend strongly on the choice of the exchange-correlation functional, the relative energetic ordering of the different terminations does not very much. Thus, the shape of the constrained Wulff construction seems to be described rather well within the chosen DFT setup.

Nevertheless, the main limitation of this approach is the constrained configurational space of considered surface terminations. As already mentioned briefly, surface reconstructions could lead to an extreme decrease in the surface free energy, which could then correspondingly show a strong influence on the overall shape of the Wulff polyhedra. Unfortunately, up to now there is no experimental information available about single crystal PdO surface reconstructions. Without any information about the periodicity or approximate composition the phase space of possible reconstructions is by far too huge to be investigated at present by *ab initio* methods alone. Here, some methodological work should be mentioned employing simulated annealing [17]

	PBE		LDA	
Orientation	Touching	10% area	Touching	10% area
Oxygen-poor:				
(001)	-54 (-45%)	-67 (-56%)	-63 (-39%)	-83 (-51%)
(110)	-40 (-47%)	-44 (-51%)	-36 (-30%)	-44 (-37%)
(111)	-7 (-10%)	-16 (-22%)	-6 (-5%)	-19 (-18%)
Oxygen-rich:				
(001)	-7 (-10%)	-42 (-58%)	-14 (-12%)	-29 (-26%)
(110)	-39 (-80%)	-41 (-84%)	-36 (-45%)	-39 (-49%)
(111)	-1 (-2%)	-20 (-37%)	-1 (-1%)	-10 (-11%)

Table 6.7: Minimum energy by which surface reconstructions at the various facets would have to lower the surface free energy, in order for the facets to touch the presently obtained constrained Wulff polyhedron (touching). Additionally, the corresponding lowering required for the facet to cover approximately 10% of the total surface area of the polyhedron is listed (10% area). All energies in meV/Å^2 (and percent changes) are given with respect to the lowest-energy (1×1) termination of the corresponding orientation.

or genetic [123–125] algorithms to reach an improved sampling in the future.

With the compiled results, though, it is still possible to get an estimate of how much the surface energy of a specific termination would have to decrease to play a significant role in the Wulff construction. Here, this is done for the three orientations (001), (110) and (111), that do not contribute to the present shape of the Wulff polyhedra in the O-poor and O-rich limit. Tab. 6.7 lists the corresponding values for each orientation, of how much the surface free energy would have to be lowered by a reconstruction (with respect to the lowest (1×1) termination in this orientation considered so far), so that the facet would just touch the current polyhedron. In addition the decrease in surface energy required for a specific orientation to significantly contribute to the Wulff polyhedra is listed. Here, a contribution is considered as being significant, if the facets of a certain termination cover approximately $10\,\%$ of the total area of the polyhedron. From the values compiled in Tab 6.7 it becomes obvious that for the (001) and (110) orientation rather massive changes in the surface free energy would have to be introduced by a possible reconstruction to show any recognizable influence on the Wulff construction, regardless of the environmental conditions (O-poor or O-rich limit) or the exchange-correlation functional (PBE or LDA). For the (111) orientation, though, only a much smaller reduction is needed, so that changes in the shape of the polyhedra are more likely with respect to this termination.

6.3.3   Stability vs. Polarity

Out of the eleven considered (1×1) terminations only the PdO(101) termination is stoichiometric, whereas all other terminations exhibit either an excess of oxygen or palladium atoms. Since oxide surfaces are often described within an ionic model, an

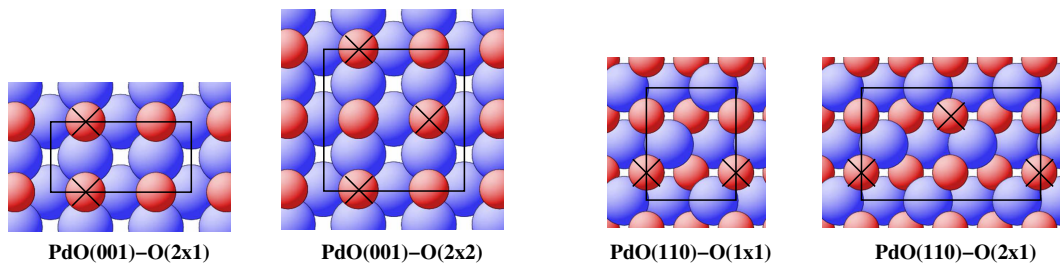PdO(001)–O(2x1)   PdO(001)–O(2x2)   PdO(110)–O(1x1)   PdO(110)–O(2x1)

Figure 6.13: Unit cells for stoichiometric reconstructions of the PdO(001)-O and PdO(110)-O terminations, achieved by simply removing the oxygen atoms marked with crosses.

unequal number of O and Pd atoms would lead to a so-called polar surface, which is traditionally not considered to be stable on electrostatic grounds [119, 120]. Theoretically, though, it has been shown that also polar oxide surfaces can indeed be stable [74, 76, 121]. Despite the known limitations of the ionic model, regarding the stability of the three different terminations in the (101) orientation (cf. Fig. 6.10) it seems to reflect very well the found stability ordering. Here, the stoichiometric PdO(101) termination has a much lower surface free energy than the polar PdO(101)-O and PdO(101)-Pd terminations. For all other low-index orientations the layer stacking is such, that it is not possible to truncate the tetragonal PdO structure in a (1×1) cell and achieve charge neutrality within the assignment of formal charges (Pd^{2+} and O^{2-}). The resulting polarity at the surface could e.g. be a reason, why the (1×1) terminations in the (001) and (110) orientation exhibit comparably high surface free energies. To investigate in a first approach the effect of the polarity on the stability of these two surface orientations, larger unit cells of the O-terminated structures are set up, where half of the oxygen atoms in the topmost layer is removed to obtain formal charge neutrality. Considering the periodicity of the surface unit cell, the remaining oxygen atoms can be arranged in two different ways for both orientations (cf. Fig. 6.13), one showing a striped pattern of full and empty rows of oxygen atoms and the other a checkerboard pattern. The surface free energies of the fully relaxed, stoichiometric surfaces are also indicated in the stability plots of the (001) and (110) orientation (Fig. 6.9 and Fig. 6.10) by the green, dashed lines. As can be seen, these stoichiometric overlayers are not at all more stable than the corresponding (1×1) O-terminated structures. These results therefore disagree with the suggestion formulated by Ciuparu *et al.* [126], that a simple removal of O atoms in the topmost layer should lead to charge compensated and thus stable PdO(001) and PdO(110) surfaces.

Obviously, formal charge neutrality does not appear to be the decisive factor in the stability of the PdO surface terminations, which is already reflected in the very low surface free energy of the polar PdO(100)-PdO termination. These findings stress the most obvious shortcoming of the electrostatic model, which is the assumption that all atoms of a certain element are identical and in the same charge state, regardless of

O-terminated	Φ (eV)	Pd-terminated	Φ (eV)	stoichiometric	Φ (eV)
PdO(001)-O	7.9	PdO(100)-Pd	4.0	PdO(101)	5.4
PdO(101)-O	7.7	PdO(001)-Pd	4.8	PdO(001)-O(2×1)	6.6
PdO(110)-O	7.2	PdO(101)-Pd	4.5	PdO(001)-O(2×2)	6.6
PdO(111)-O	5.9	PdO(110)-Pd	4.4	PdO(110)-O(1×1)	5.9
		PdO(111)-Pd	4.7	PdO(110)-O(2×1)	5.8

PdO-terminated	Φ (eV)
PdO(100)-PdO	6.4

Table 6.8: Work function of the 11 different (1×1) PdO surface terminations and the 4 stoichiometric terminations of the (001) and (110) termination with larger surface unit cells considered in this work. All values are in eV. PBE is used as exchange-correlation functional.

whether they are e.g. in the bulk or at the surface. It has been shown, though, that structural and electronic relaxation at the surface can significantly change this simple picture [74, 76]. Other factors like an appropriate excess stoichiometry at oxygen-rich conditions might then become more important than the polarity issue.

Nevertheless, regarding the work functions of the different PdO surface terminations (cf. Tab. 6.8) it can be seen, that there is actually a notably different surface dipole moment associated with the different terminations. Focussing first on the (1×1) terminations the calculated work functions fit actually quite well to the ionic model. The work function of the stoichiometric PdO(101) termination exhibits a medium value of 5.4 eV, whereas the work functions of all Pd-terminated surface are 0.6–1.4 eV lower and the work functions of the O-terminated surfaces are 0.5–2.5 eV higher. Remarkable is the comparably low work function of the PdO(111)-O termination. This can be explained by the rather dense stacking in the (111) direction and the resulting small interlayer distance between the topmost oxygen layer and the second layer Pd atoms of only 0.51 Å, which can then lead to a smaller dipole moment and respectively smaller work function. Also the work functions of the stoichiometric (001) and (110) superstructure terminations fit nicely into this scheme. Compared to their corresponding O-terminated surfaces a clear decrease in the work function of 1.1–1.4 eV can be observed, i.e. the stoichiometric surfaces have a smaller surface dipole moment. As discussed before though, the stability is not enhanced in these stoichiometric surface terminations.

Apparently, the polarity is not the main factor in determining the stability of the PdO surfaces. As a next step a possible correlation between the stability and the binding energy of the surface oxygen atoms is investigated, since the most stable (1×1) termination of a specific orientation has always O atoms in the topmost layer. The binding energies with respect to gas phase O_2 are given in Tab. 6.9. Indeed the binding energies of the topmost oxygen atoms show a clear correlation to the found stability ordering. The PdO(100)-PdO and PdO(101) terminations, which solely build up the

Surface termination	Binding energy (eV)	Coordination
PdO(100)-PdO	-2.4	3
PdO(101)	-2.3	3
PdO(111)-O	-1.8	2
PdO(110)-O	-1.6	2
PdO(001)-O	-1.3	2
PdO(101)-O	0.5	1

Table 6.9: Binding energy of the topmost oxygen atom of the low-index PdO surfaces with respect to the O_2 molecule. In addition the number of Pd atoms, to which the corresponding O atom is coordinated, are listed.

Wulff construction, also exhibit the most strongly bound surface oxygen atoms. Also the binding energies of the other terminations clearly reflect their surface stability. The PdO(111)-O termination, which is already very close to contribute to the equilibrium Wulff construction, has actually also the third most strongly bound surface oxygen atoms.

In addition the binding energies can be connected to the coordination of the surface atoms. In PdO bulk the oxygen atoms are tetrahedrally surrounded by four palladium atoms. In the two most stable terminations, PdO(100)-PdO and PdO(101), the oxygen atoms are still coordinated to three palladium atoms, whereas in the intermediate stable structures, PdO(111)-O, PdO(110)-O and PdO(001)-O, the O atoms are only coordinated to two Pd atoms and in the rather unstable PdO(101)-O termination to one Pd atom. Thus, the stability of the studied (1×1) terminations seems to be primarily determined by the openness of the surface orientation, i.e. if the surface structure exhibits highly coordinated oxygen binding sites.

6.4   Conclusions

The *ab initio* atomistic thermodynamics approach is used to obtain a first insight into the structure and composition of the Pd(100) surface in contact with an oxygen gas phase. Within this approach the stability of different surface phases can be compared over a wide temperature and pressure range of the surrounding gas phase.

There are, however, several uncertainties in the obtained results introduced by the accuracy in the total energies, determined by the employed basis set and exchange-correlation functional, by the approximations in evaluating the thermodynamic functions, mainly due to the vibrational contribution to the Gibbs free energy, as well as by the restricted sampling of the configurational space. A detailed discussion of the different factors shows, that for comparing the stability range of the different oxidation stages of the Pd(100) surface (clean, adlayers, surface oxide, bulk oxide) the exchange-correlation functional induces the largest uncertainty, whereas for determin-

ing the equilibrium shape of a PdO single crystal the sampling of the configurational space is the limiting factor.

Considering the stability of different adlayer structures and the $(\sqrt{5} \times \sqrt{5})R27°$ surface oxide there are, nevertheless, some conclusions, that are not affected by the choice of the exchange-correlation functional. It is found, that the $c(2 \times 2)$ oxygen adlayer on Pd(100) does not appear as stable phase over the investigated temperature and pressure range, although this structure has been frequently observed in UHV experiments. This suggests that the $c(2 \times 2)$ phase is a meta-stable state, which only forms due to the adsorption kinetics. Furthermore it can be seen that the $(\sqrt{5} \times \sqrt{5})R27°$ surface oxide is a stable phase over an extended (T, p)-range regardless of the chosen exchange-correlation functional. Thus, the surface oxide can be regarded as separate phase, clearly distinguished from the bulk oxide and adlayer structures. The actual position of the boundaries between the different phases in the (T, p)-space, though, does strongly depend on the exchange-correlation functional (cf. Fig. 6.6). Comparing the PBE and RPBE results there is an uncertainty in the phase boundaries of as much as ~ 4 orders of magnitude in pressure and $\sim 200\,\mathrm{K}$ in temperature. Comparing the two extremes in the employed exchange-correlation functionals, the LDA and the RPBE, the uncertainty is even larger with ~ 10 orders of magnitude in pressure and $\sim 450\,\mathrm{K}$ in temperature.

The determined equilibrium shape of a PdO single crystal appears not to be affected that much by the uncertainty arising from the exchange-correlation functional. In both, the PBE and LDA, the same low-index surfaces contribute to the equilibrium shape and the same surface termination forms the dominant facet. In contrast to the traditional assumption, that so-called polar surface are rather unstable (which is based on an ionic description of oxide surfaces), for the low-index PdO surface terminations the polarity does not have any significant influence on the stability. It is rather the coordination of the first-layer oxygen atoms that appears to be decisive for the stability. A much large uncertainty in the equilibrium shape of the PdO single crystal is introduced by the restricted configurational sampling. Possible surface reconstructions leading to a lowering of the surface energy of a certain surface orientation could notably change the equilibrium shape. However, an estimate of how much a reconstruction would have to influence the corresponding surface energy is given.